Giant renormalization of the quasiparticle dispersion in degenerately doped graphene nanoribbons

B.V. Senkovskiy,*,† A. Fedorov,†,‡ D. Haberer,¶ M. Farjam,§ K.A. Simonov,∥,⊥

A.B. Preobrajenski, N. Mårtensson, N. Atodiresei, V. Caciuc, S. Blügel, A. Rosch, $^{@}$ N.I. Verbitskiy, $^{\dagger,\triangle,\nabla}$ M. Hell, † D.V. Evtushinsky, †† R. German, † T. Marangoni, P.H.M. van Loosdrecht, F.R. Fischer, and A. Grüneis*, II. Physikalisches Institut, Universität zu Köln, Zülpicher Strasse 77, 50937 Köln, Germany, St. Petersburg State University, St. Petersburg, 198504, Russia, Department of Chemistry, University of California at Berkeley, 699 Tan Hall, Berkeley, CA 94720, U.S.A., School of Nano Science, Institute for Research in Fundamental Sciences (IPM), P.O. Box 19395-5531, Tehran, Iran, Department of Physics and Astronomy, Uppsala University, Box 516, 75120, Uppsala, Sweden, MAX IV, Lund University, Box 118, 22100 Lund, Sweden, Peter Grünberg Institute and Institute for Advanced Simulation, Jülich, Germany, Institute of Theoretical Physics, Universität zu Köln, Zülpicher Strasse 77, 50937 Köln, Germany, Faculty of Physics, University of Vienna, Strudlhofgasse 4, A-1090 Vienna, Austria, Department of Materials Science, Moscow State University, Leninskiye Gory 1/3, 119992, Moscow, Russia, and Helmholtz-Zentrum Berlin für Materialien und Energie, Elektronenspeicherring BESSY II, Albert-Einstein-Strasse 15, 12489 Berlin, Germany

E-mail: senkovskiy@ph2.uni-koeln.de; ffischer@berkeley.edu; grueneis@ph2.uni-koeln.de

Abstract

Charge transfer doping of semiconducting N=7 armchair graphene nanoribbons by lithium causes drastic changes in its electron and phonon system. Using angle-resolved photoemission spectroscopy and scanning tunneling spectroscopy we observe a quasiparticle band gap renormalization from 2.4 eV to 2.1 eV. The effective mass of the conduction band carriers increases by a factor of four to a value equal to the free electron mass. The band gap and mass renormalization also affect the Raman spectra. Raman measurements of lithium doped nanoribbons show a loss in intensity, a shift of the Raman frequencies and an absence of a Kohn anomaly at the Brillouin zone center. Near-edge X-ray absorption fine structure measurements shows that upon doping the antibonding π^* states are filled with electrons. These results highlight that doping of a semiconducting 1D system is strikingly different from its 2D or 3D counterparts. The effective mass increase by doping is a means to enhance the density of states at the Fermi level which can have palpable impact on the transport and optical properties. The present work introduces alkali metal doped graphene ribbons as a new tunable quantum material with high potential for basic research and applications.

KEYWORDS: graphene, graphene nanoribbons, nanowires, ARPES, Raman, STS, electronic band structure, density-functional theory, chemical doping

^{*}To whom correspondence should be addressed

[†]II. Physikalisches Institut, Universität zu Köln, Zülpicher Strasse 77, 50937 Köln, Germany

[‡]St. Petersburg State University, St. Petersburg, 198504, Russia

[¶]Department of Chemistry, University of California at Berkeley, 699 Tan Hall, Berkeley, CA 94720, U.S.A.

[§]School of Nano Science, Institute for Research in Fundamental Sciences (IPM), P.O. Box 19395-5531, Tehran, Iran

Department of Physics and Astronomy, Uppsala University, Box 516, 75120, Uppsala, Sweden

¹MAX IV, Lund University, Box 118, 22100 Lund, Sweden

[#]Peter Grünberg Institute and Institute for Advanced Simulation, Jülich, Germany

[®]Institute of Theoretical Physics, Universität zu Köln, Zülpicher Strasse 77, 50937 Köln, Germany

[△]Faculty of Physics, University of Vienna, Strudlhofgasse 4, A-1090 Vienna, Austria

 $[\]nabla$ Department of Materials Science, Moscow State University, Leninskiye Gory 1/3, 119992, Moscow, Russia

^{††}Helmholtz-Zentrum Berlin für Materialien und Energie, Elektronenspeicherring BESSY II, Albert-Einstein-Strasse 15, 12489 Berlin, Germany

Introduction

Strong many-body effects in one-dimensional (1D) systems yielded numerous breakthroughs such as Tomonaga-Luttinger liquid behavior in carbon nanotubes¹, spin-charge separation in $SrCuO_2^2$, Peierls distortion in atomic wires³ and an optical response in nanotubes that is dominated by excitons⁴. As a consequence, the study of 1D materials is one of the major research directions in condensed-matter physics. In 1D semiconducting graphene nanoribbons (GNRs) the inclusion of electron-electron interactions in electronic structure calculations leads to a larger quasi-particle (QP) band gap⁵⁻⁷, which is significantly reduced by screening from a metallic substrate⁸. Many-body interactions in GNRs also give rise to prominent excitonic effects⁹. If the charge carrier density is increased via doping, one might intuitively expect stronger screening which could lead to a smaller band gap. Doping of GNRs could thus be an efficient tool to manipulate and control their many-body interactions and their optical and electronic properties. Indeed, for carbon nanotubes there is experimental evidence of a QP band gap renormalization $^{10-13}$. Carbon nanotubes are archetypical 1D materials but, despite a 20-year history, the large-area synthesis of long and monochiral carbon nanotubes remains challenging ¹⁴. Their parent compound, two-dimensional (2D) graphene can be easily grown over cm² areas¹⁵ and its large single-crystalline domains allow for precise measurements. GNRs combine the best attributes of the nanotube and graphene worlds. They are 1D materials plus they exist as highly uniform monochiral samples thanks to bottom-up nanofabrication techniques ^{16–23}. The ability to tune the band gap in semiconducting GNRs by varying the ribbon width 19,24-26 and the ease of producing high-quality ohmic contacts makes them perfectly suited for production of nanoscale devices ^{27–31}. The unprecedented structural quality of massively parallel ribbons grown on vicinal surfaces and their flatness opens up the use of powerful spectroscopic methods such as angle-resolved photoemission spectroscopy (ARPES)^{8,32}. Poor sample homogeneity has been preventive in applying these techniques for nanotubes up to now. Atomic wires have been studied using ARPES^{3,33} but the presently studied semiconducting GNRs are different from atomic wires in the sense that GNRs have widely tunable electronic properties. Their width can be varied and they are susceptible to chemical doping as will be shown in this manuscript.

So far chemical doping of GNRs has been mainly realized by two routes. One route is functionalization of the edges^{34–39} and the other route is by substitutional doping of the precursor molecule ^{21,40,41}. Much less is known regarding the doping of graphene nanoribbons by alkali metals, despite its great success to induce large electron-phonon coupling 42,43 and even superconductivity 44,45 in graphene and to elucidate Tomonaga-Luttinger liquid behavior in nanotubes 46. Here we show directly, using ARPES, that Li doping of the N=7 armchair graphene nanoribbon (7-AGNR) leads to a significant reduction of the QP band gap and a giant renormalizations of the effective mass by a factor of four during a semiconductorto-metal transition. The vibrational properties are also strongly affected and we observe a shift of the ribbon specific Raman modes and a transition from resonance to off-resonance Raman. The unique experimental approach using a combination of ARPES, scanning tunneling spectroscopy (STS), ultra-high-vacuum (UHV) Raman spectroscopy and near edge X-ray absorption fine structure (NEXAFS) spectroscopy techniques is a key that allows us to gather an eclectic picture of the physical and chemical properties of Li doped GNRs. The experimental data are compared against density-functional theory (DFT) calculations of the electron energy band structure without explicit inclusion of many-body interactions.

Sample characterization

7-AGNRs were synthesized using the well-established bottom-up fabrication approach on Au surfaces 17,32 . Figure 1(a) depicts the scanning tunneling microscopy (STM) topographic images of 7-AGNRs on a Au(788) surface. The vicinal surface of Au(788) with regular arrays of narrow (111) terraces imposes restrictions on the direction of growth and yields a homogeneous surface of densely aligned ribbons. The STM images reveal excellent nanoribbon alignment over scan regions of up to 500 nm \times 500 nm (see supplementary information).

In order to confirm the alignment for larger areas we employ low-energy electron diffraction (LEED). Figure 1(b) depicts a LEED image, confirming ordering over areas of about 10 μ m² (the size of the electron beam spot). Changing of the position of the spot on the 1 cm² crystal does not affect the LEED pattern which means that the alignment area is limited only by the crystal size. According to the well-known LEED pattern of $\mathrm{Au}(788)^{47}$ we determined the near vertical orientation of the (111) terraces along the [0 1 1] crystallographic direction. Diffraction from 7-AGNRs represents a hexagonal structure rotated relatively to the Au diffraction spots by an angle of 30°. This can be expressed in terms of the parent graphene unit cell, which in contrast to the infinite graphene layer on Au(111) with dominant R0 orientation ^{48,49} forms a R30 orientation [see Figure 1(c)]. The good alignment of the nanoribbons allows to probe their optical anisotropy in polarized Raman measurements. Due to the 1D nature of GNRs their optical response is dominated by a series of van Hove singularities (VHSs). Using a matching laser energy one can excite resonantly optical transition between two VHSs. The E_{22} optical transition energy for 7-AGNRs/Au(788) was experimentally found to be equal to 2.3 eV⁹. We have taken advantage of the large optical response at the VHSs to perform resonance Raman spectroscopy measurements with 532 nm (~ 2.33 eV) laser. Figure 1(d) depicts Raman spectra of 7-AGNRs on Au(788) with the polarization parallel and perpendicular to the axis of the nanoribbons. The scattering geometry is shown in the inset Figure 1(d). Here we use the Porto notation, e.g. z(y,y)zindicates that the incident and scattered light propagate in z direction and the incident and scattered light are polarized along the y direction, i.e. along the direction parallel to the terraces (Au[0 1 $\bar{1}$]). Similarly z(x,x)z indicates a polarization of incident and scattered light perpendicular to the terraces. From Figure 1(d) it can be seen that the Raman intensity ratio for z(y,y)z and z(x,x)z is equal to ~ 10 . It is clear that the GNRs are aligned almost perfectly parallel to the terraces. The observed anisotropy is governed by the dipole selection rules 50 which state that for armchair nanoribbons the \mathbf{E}_{ii} optical transition is allowed only for the light polarized along the ribbon axis. Another factor that affects the intensity is the depolarization effect which strongly suppresses the absorption of the perpendicularly polarized light⁵¹. For assignment of the experimentally observed Raman peaks of 7-AGNRs to phonon eigenvectors we have performed calculations using a force constant model and bond-polarizability theory^{52,53}. The obtained results are shown in the supplementary information and are consistent with previously published data⁵³.

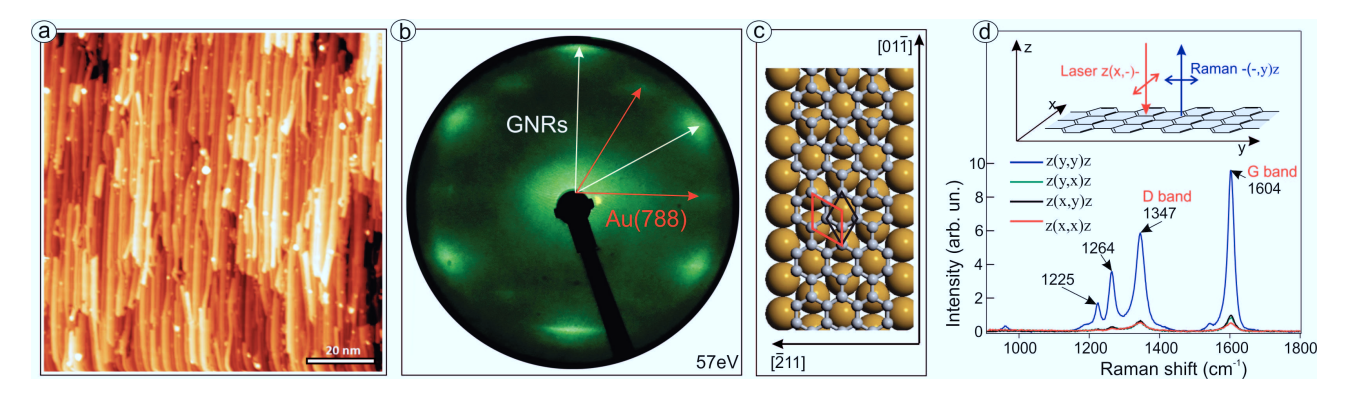


Figure 1: (a) STM topographic image of aligned 7-AGNRs on Au(788). $V_s = 0.6$ V and $I_t = 40$ pA. (b) LEED pattern of 7-AGNRs/Au(788) obtained with an electron beam energy 57 eV. (c) Sketch of the 7-AGNR oriented along the Au(111) terrace. The parent graphene unit cell (black) is rotated to the unit cell of the Au surface (red) by 30°. (d) Polarized Raman spectra of aligned 7-AGNRs on Au(788) measured in 180° back scattering geometry. The blue (red) spectrum corresponds to light polarization along (perpendicular) to the step edges of the Au(788) surface. The exciting laser wavelength was 532 nm.

Results

Angle-resolved photoemission and X-ray absorption spectroscopy

Figure 2 shows the raw ARPES intensity maps (top image) measured in the direction parallel to the axis of 7-AGNRs uniformly aligned on Au(788) surface and the second derivative (bottom image) of the ARPES intensity. The second derivative method is commonly used to enhance the band maxima. Three parabola-like electronic valence sub-bands of pristine 7-AGNRs can be clearly seen in Figure 2(a) (Ref. 8). Using parabolic fits of the ARPES maxima we determined the position of the valence band maximum (VBM) E_{V1} =0.88eV and the effective mass at the VBM m_{V1}^* =-0.23 m_e (here m_e indicates the free electron mass).

The position of E_{V1} is in good agreement with values reported previously: 0.87 eV (Ref. 32) and 0.7 eV (Ref. 8). Our value for m_{V1}^* is in good agreement to the work of Ref. 8 ($-0.21m_e$) but a factor 5 smaller than the result of Ref. 32 ($-1.07m_e$). This discrepancy may be due to the fact that our study was carried out using synchrotron light with high energy resolution as compared to the Ref. 32.

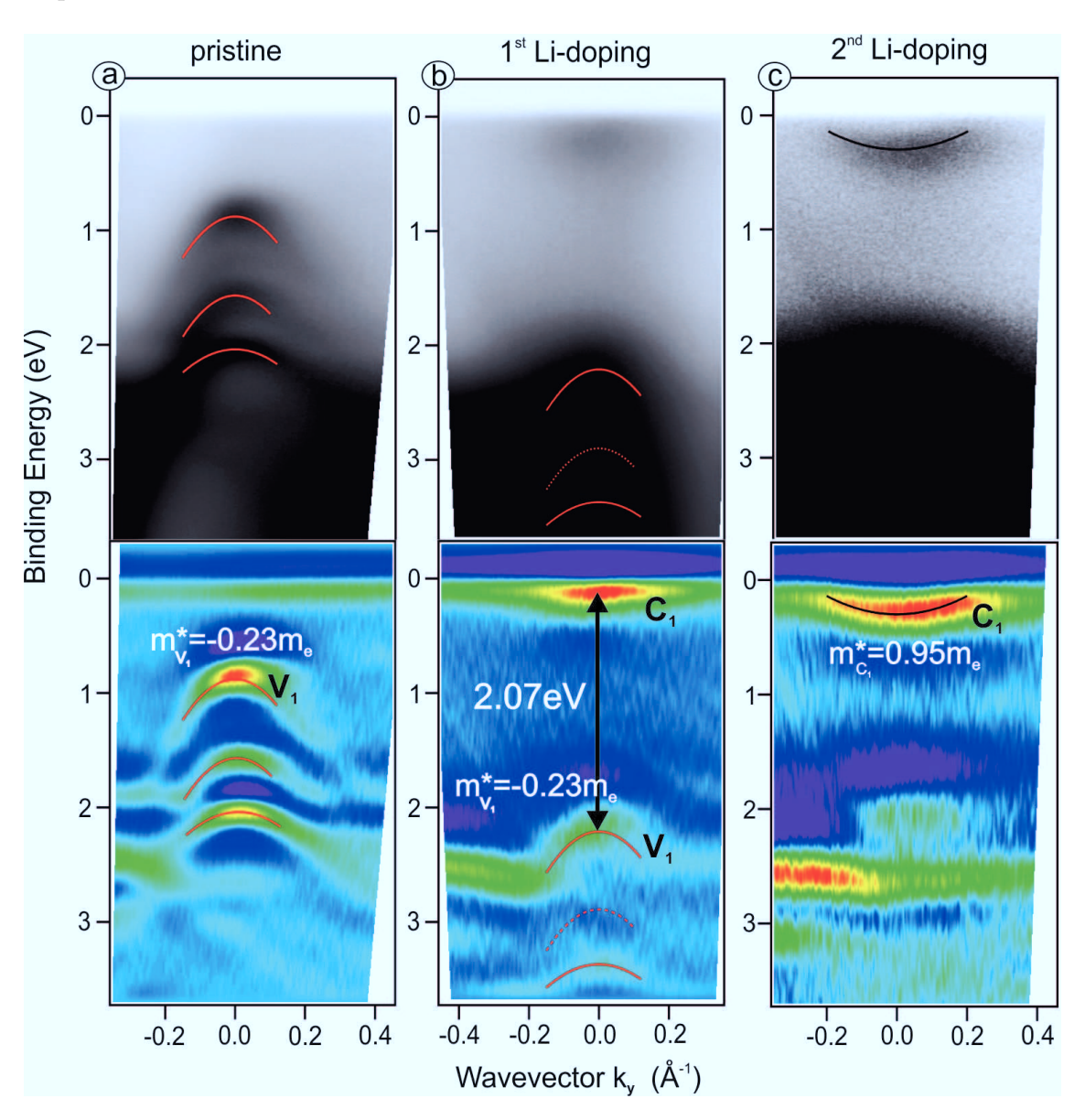


Figure 2: ARPES spectra of aligned 7-AGNRs on Au(788) accumulated along the k_y , where k_y was measured with respect to the second Brillouin zone: (a) pristine 7-AGNRs, (b) after 1^{st} Li-doping at room temperature and (c) after 2^{nd} Li-doping. The top row represents raw data, the bottom row their second derivatives.

Figure 2(b) shows that after in-situ deposition of one monolayer (ML) of Li the valence band shifts down by 1.33±0.05 eV and higher photoemission intensity appears at the Fermi level. This feature is assigned to the conduction band of Li doped 7-AGNRs and its observation constitutes a proof of the semiconductor-to-metal transition induced by Li deposition. The occupation of the conduction band allows to measure a value of the energy separation between valence and conduction bands by ARPES and we obtain a value of 2.1 eV. Interestingly this value is significantly lower than the band gaps measured by STS of 7-AGNRs on Au(111). Previously reported values of the band gap were 2.7 eV (Ref. 18), 2.3 eV (Ref. 8), 2.5 eV (Ref. 19) and 2.37 eV (Ref. 54). Let us now look to the effective carrier masses. In order to have a higher doping to reliably fit the effective mass value to experiment, we have performed a second deposition of Li. Figure 2(c) shows the corresponding ARPES spectra and their second derivative which clearly exhibit a parabola-like feature. This is the maximum doping level we achieved and the area of the 1D Brillouin zone (BZ), occupied by the conduction band below the Fermi level suggests the doping level is about 1.5 ± 0.1 electrons per nm. The parabola-like dispersion of the conduction band C_1 corresponds to a giant effective mass of 0.95 ± 0.05 m_e. From zone-folding we expect electron-hole symmetry in the electronic structure of 7-AGNRs. Thus the absolute valus of the effective masses should be close to one another and this is also consistent with DFT results $^{55-57}$ and STS data⁵⁴. This is a dramatic QP effective mass renormalization by a factor of four induced by electron doping and could be related to strong electronic correlations that are present in 1D systems ^{12,58}. Finally, we also performed X-ray photoemission spectroscopy (XPS) measurements to explore the C 1s core-levels and to analyze the changes in the chemical state of 7-AGNRs upon Li doping. A survey XPS spectrum also confirms the absence of an O is peak at around 530 eV indicating a clean sample surface. These data are shown in the supplementary information.

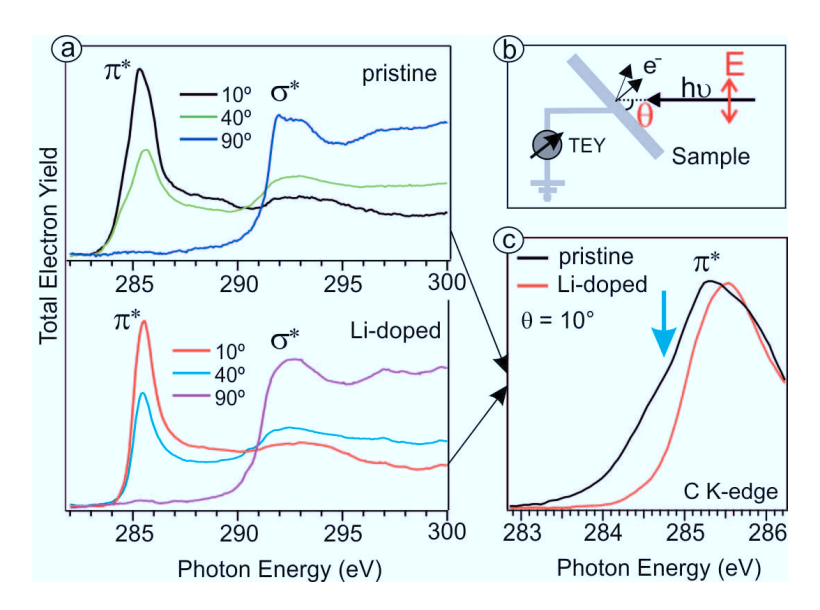


Figure 3: (a) Angle-dependent NEXAFS spectra of 7-AGNRs/Au(788) at the C K-edge obtained in the total electron yield (TEY) mode before and after Li doping. (b) Sketch of the NEXAFS experiment, where θ is the angle between the direction of incidence of linearly polarized radiation and the sample surface. (c) Close-up of the NEXAFS spectra of (a) around the π^* resonance at grazing angle $\theta = 10^{\circ}$. The blue arrow indicates the disappearance of the low-energy shoulder after Li-doping.

Near edge X-ray absorption fine structure spectroscopy

To investigate possible structural distortions of the 7-AGNRs as a result of Li adsorption we performed a NEXAFS spectroscopy study of pristine and doped samples. Moreover, NEXAFS is able to proof the π character of the conduction band. The series of C K-edge absorption spectra of 7-AGNRs are shown in Figure 3(a). A sketch of the experimental geometry is depicted in Figure 3(b). The angle-dependent behavior of the π^* and σ^* resonances suggests a planar structure of ribbons before and after Li deposition. Figure 3(c) shows a zoom of the π^* region of the NEXAFS spectrum illustrated in Figure 3(a). The low-energy shoulder of the π^* resonance is clearly visible in the NEXAFS spectrum of pristine GNRs. However, upon Li deposition it disappears. This is because the transition from the C1s core level to the lowest conduction band states is not possible after doping. Due to the element-specific nature of the NEXAFS method, this gives a proof of the occupation of the C derived π^* levels.

Scanning Tunneling Spectroscopy

We measured the energy band gap E_g of 7-AGNRs on Au(788) by STS in order to compare it to the valence-conduction band separation measured by ARPES of Li doped 7-AGNRs on Au(788). The values of E_g for doped and pristine GNRs can be compared to each other and their difference will yield the doping induced changes. Our analysis relies on the fact that STS and ARPES reveal identical energy band dispersions which has been explicitly shown for GNRs⁵⁹. A similar approach of comparing STS derived quasiparticle band gaps and photoluminescence derived optical band gaps in MoSe₂ monolayers on Au has yielded the exciton binding energies directly ⁶⁰. In the present case, the differences between the band gaps obtained by ARPES and STS is equal to the self-energy corrections due to charge transfer doping by Li and can directly be compared to the theoretical predictions. It is important to point out that a precise STS measurement of Li doped nanoribbons is hampered by the prohibitively high Li mobility.

The combined set of experimental STM and STS data for aligned 7-AGNRs on Au(788) surface are shown in Figure 4(a,b). The STS spectra show easily discernible peaks around the Fermi level corresponding to the first sub-bands V_1 and C_1 . The value of E_g is estimated as the difference between the leading edges of the valence and conduction band related peaks in the STS spectra. We have measured STS at various locations along several ribbons and found reproducible values of E_g . Close to a bias voltage of zero, there are features in the dI/dV spectra due to the Au surface states 19. It can be seen that a value of $E_g = 2.4\pm0.1$ eV is consistent with all measured points. Notably this value is in good agreement to the reported gap values for 7-AGNRs on Au(111)^{8,19,54} [See also supplementary information for STS data of 7-AGNRs on Au(111)]. This is not surprising as the terraces of the vicinal Au(788) surface have an (111) structure. The small observed deviations might be due to the stronger inter-ribbon interactions in the denser packed Au(788) surface. In the Raman section we will provide more evidence of stronger inter-ribbon interactions on Au(788). Our STS data provide a larger QP band gap of as compared to the ARPES measurements. The

supplementary information provides a direct comparison of the dI/dV curve versus second derivative energy distribution curve. Thus the Li doping reduces the QP band gap by more than 300 meV and does not provide a rigid band shift. Together with the mass increase as observed in the previous section, the bands are substantially renormalized by Li doping. Figure 4(c) depicts a sketch of the experimentally observed QP bands before and after Li doping.

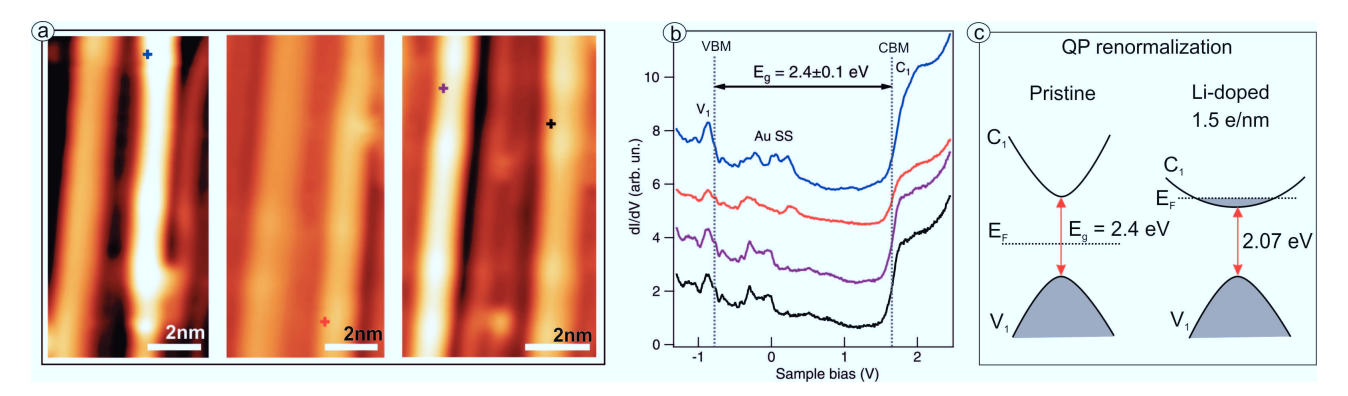


Figure 4: (a) STM topographic images of aligned 7-AGNR on Au(788) (left: $V_s = 0.6$ V, $I_t = 150$ pA, middle: $V_s = 0.6$ V, $I_t = 100$ pA, right: $V_s = 0.6$ V, $I_t = 130$ pA). Colored crosses in the STM images indicate the position where the STS spectra were measured. (b) dI/dV point spectra ($V_{mod} = 10$ mV) obtained from several different 7-AGNRs on Au(788) depicted in (a). The dotted lines mark the onsets of valence band maximum and conduction band minimum, yielding an electronic band gap of $E_g = 2.4 \pm 0.1$ eV. Spectra are offset for clarity. (c) Sketch of the observed QP renormalization in Li doped 7-AGNRs.

Density functional theory

To explain possible reasons for the observed electronic structure renormalizations, we have performed DFT calculations to optimize the geometry and compute the electron energy band structure of pristine and Li doped 7-AGNRs for various Li adsorption sites. Figure 5(a) depicts the DFT calculated 1D electron energy bands of pristine 7-AGNRs along with the unit cell of a 7-AGNR with 14 carbon atoms. Figure 5(b,c) show the DFT calculated band structure of Li doped 7-AGNRs. The configuration we consider in Figure 5(b) is one where the Li is placed above the center benzene ring of an anthracene unit. The second configuration shown in Figure 5(c) is one where two Li atoms are placed above the edge

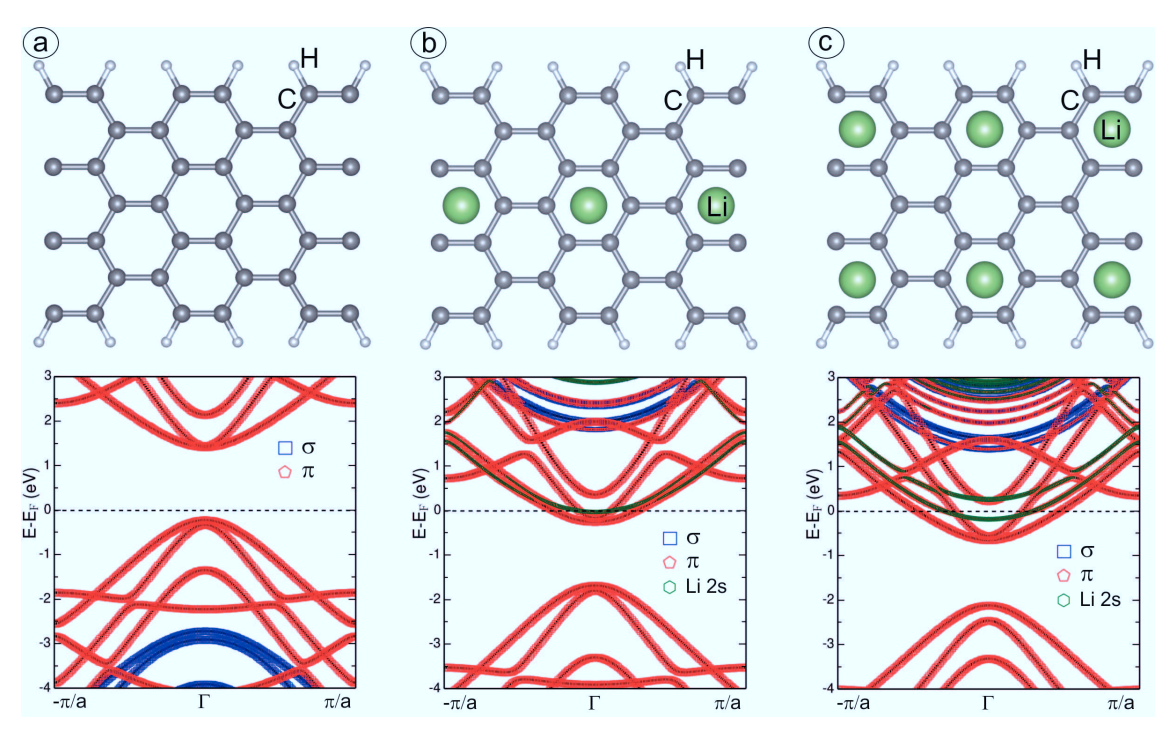


Figure 5: Electronic energy band structure and unit cell of (a) pristine and (b,c) Li doped 7-AGNRs. The labels V_1 (V_2) and C_1 (C_2) depict the first (second) valence and conduction bands, respectively. The red (blue) color indicates a π (σ) character of the respective band. Green depicts the electronic bands with Li character.

benzene rings of the anthracene unit. In the supplementary information we also show several other possible configurations. However, judging from the experimentally observed band structure, the most relevant configuration is the first one with one Li atom per 7-AGNR unit cell. It can be seen from Figures 5(b) that the interaction of Li with the 7-AGNR leads to a complete electron transfer from Li to the nanoribbon. This causes the occupation of the lowest conduction bands and a transition from a semiconductor to a metal. The Li derived band is above the Fermi level. Further doping by increasing the Li/C stoichiometry causes more charge transfer and a larger shift of the Fermi level [see Figure 5(c)]. We have performed parabolic fits of the effective masses to V_1 and C_1 for all configuration shown in Figure 5. We find an effective mass $m_{C_1}^* = 0.55m_e$ for the pristine system. For the two doped systems we find $m_{C_1}^* = 0.62m_e$ and $m_{C_1}^* = 0.55m_e$ for the one and two Li atoms per unit cell, respectively. The valence band mass for the pristine 7-AGNR is $m_{V_1}^* = 0.41 m_e$. For the doped 7-AGNRs, we have masses of $m_{V_1}^* = 0.40m_e$ and $m_{V_1}^* = 0.39m_e$ for the configurations with one and two Li atoms per unit cell, respectively. This indicates that, according to DFT, $m_{V_1}^*$ and $m_{C_1}^*$ are close to one another and not significantly perturbed by Li doping. Hence the experimentally observed increase in $m_{C_1}^*$ is strikingly higher. This effect is apparantly not captured by the DFT calculation. Regarding the VB-CB separation, we calculated a value of E = 1.64 eV for the pristine system. For the doped systems we find E = 1.43 eV and E = 1.47 eV for one and two Li atoms per unit cell, respectively. It is clear that DFT predicts that the Li doping is slightly reducing the VB-CB separation. Indeed our experiments are consistent with this tendency.

Ultra-high-vacuum Raman spectroscopy

To investigate the effect of electron doping by alkali metals on the vibrational spectrum of 7-AGNRs we performed in-situ Raman measurements of Li doped GNRs in a specially built UHV Raman chamber. Figure 6(a) depicts a sketch of the setup and indicates the laser path. The UHV Raman spectra of 7-AGNRs on Au(111) and Au(788) before and after

deposition of Li are shown in Figure 6(b). Using UHV Raman we have also verified that the Li doping of GNRs is fully reversible upon annealing the sample (see supplementary information). This property of Li doping is important for future use of GNRs in battery applications. After Li doping, a reduction in the Raman intensity by a factor of ~ 20 is observed. The unique combination of UHV Raman and ARPES measurements on identical samples allows us to elucidate the reason of the observed Raman intensity loss. Looking to the ARPES spectrum of Figure 2(b, c) it is clear that the C_2 band is not occupied and therefore the E_{22} transition is not blocked by the Pauli exclusion principle. The observed intensity loss therefore must have a different origin. The resonance condition for optical absorption at E_{22} is determined by the effects of both the QP gap and the exciton binding energy. Their combined effects shift the E_{22} resonance away from the original position. This leads to a change from resonance to off-resonance Raman. Another factor that seems to influence the Raman energies is the ribbon density. The ribbons are more dense on Au(788) as compared to Au(111). To stress this point we have included STM images of 7-AGNRs synthesized on Au(111) in the supplementary information. Interestingly, the Raman modes of pristine ribbons on Au(788) are blue-shifted relative to the ribbons on Au(111) as a result of the higher density and hence larger inter-ribbon interaction. This situation is analogous to the blue-shift of the radial breathing mode in carbon nanotube bundles compared to isolated carbon nanotubes⁶¹. Li doping seems to decrease the inter-ribbon interaction and results in Raman peaks for ribbons on Au(111) and Au(788) substrates that are very close to one another.

Regarding the phonon energy renormalization for 7-AGNRs on Au(111) we observe that Li doping induces an energy upshift for the G peak by 4 cm⁻¹ while the D peak and the peak at 1260 cm⁻¹ are downshifted by up to 8 cm⁻¹ (the intensity of the peak at 1221 cm⁻¹ is too weak to make a statement regarding its shift). We rationalize the observed Raman shifts in terms of effects beyond the adiabatic Born-Oppenheimer approximation⁶², Kohn anomalies in the phonon dispersion relation^{63,64} and the lattice expansion resulting from the filling of

anti-bonding states 65 . Kohn anomalies and the lattice expansion lead to a a downshift of the energies of optical phonon branches. The Kohn anomalies affect phonon wavevectors $q=2k_F$, where k_F is the Fermi wavevector, while the lattice expansion and consequent weakening of the force constants affects all phonons and hence all observed Raman modes. The breakdown of the Born-Oppenheimer approximation causes a phonon energy $upshift^{62}$. It depends on the electronic structure of the sp² carbon material, the phonon branch and wavevector, and on the doping level which of these competing factors prevails. For example for graphene, in its pristine state a semi-metal, doping by electrons causes an upshift of the GRaman band because the Kohn anomaly at $q = \Gamma$ disappears upon doping ⁶⁴. The situation in 1D ribbons is different. Unlike graphene, ribbons are intrinsically semiconductors and do not exhibit a Kohn anomaly prior to doping. Upon doping we therefore expect that a Kohn anomaly appears at $q_y=2k_F$ (for a single metallic band). Due to the shallow band and the high effective mass $2k_F$ assumes large values of $2k_F \sim 0.5 \text{Å}^{-1}$ [see Figure 2(c)]. This is why the Kohn anomaly does not affect Γ point phonons and the Raman G band exhibits a surprising stiffening which we ascribe to non-adiabatic effects, i.e. the interaction of the 1D electron gas with C-C bond stretching vibrations along the axis of the ribbon. In regards to the downshift of the other phonon modes we ascribe this to the dominance of lattice expansion.

Discussion

Let us start by discussing the origin of the observed changes in the band gap and the effective mass. Apparently these changes stem from the effects of an increased electron concentration, the presence of positive Li ions and many-body effects in 1D ribbons. DFT is able to describe well the reduction of the band gap with Li doping. A similar situation is observed in semiconducting nanotubes. Here a band gap reduction was found when field effect doping of nanotubes was performed ^{10–13}. However, DFT fails completely to describe

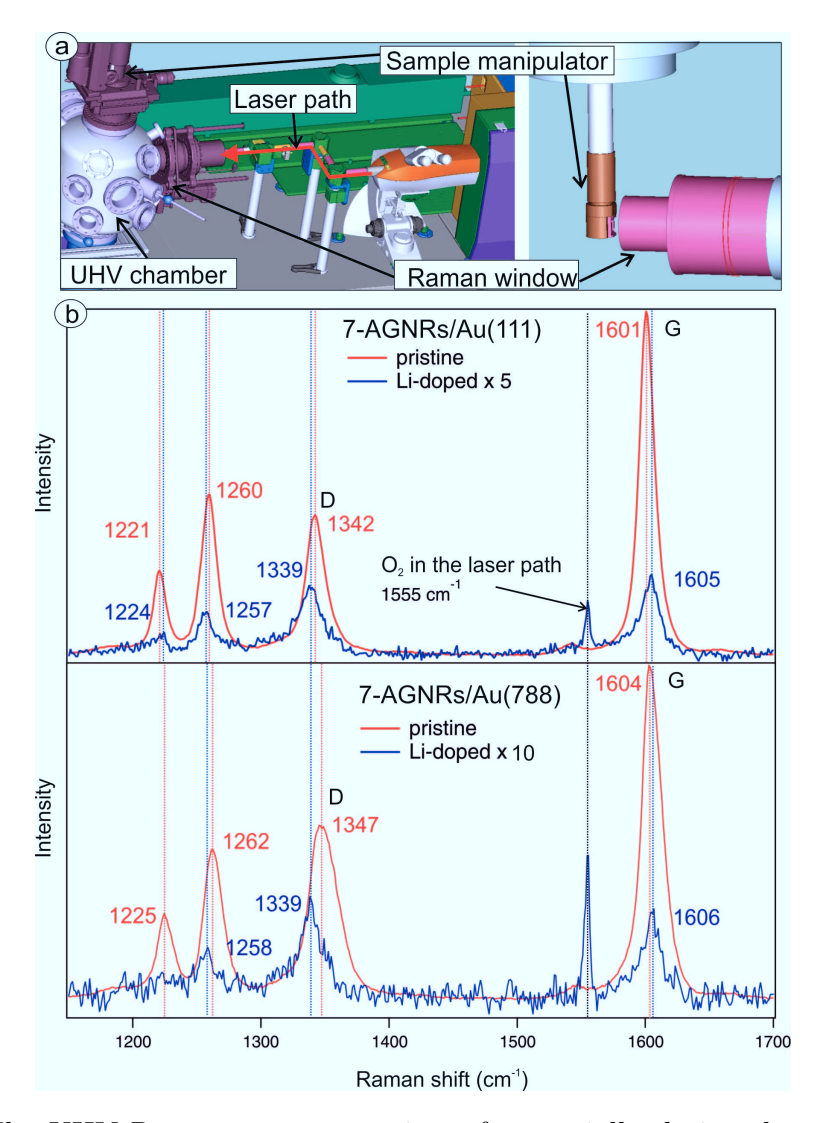


Figure 6: (a) The UHV Raman system consists of a specially designed optical flange that connects a commercial Raman setup with an UHV system. The sample is mounted on a motorized manipulator. (b) UHV Raman spectra of 7-AGNRs on Au(111) and on Au(788) measured before and after Li deposition with a 532 nm laser.

the increase of the effective mass that we observed in the ARPES data. It has been put forward that the reason of the observed effective mass renormalization upon a transition to a 1D metallic state in nanotubes is the presence of acoustic charge carrier plasmons, which have a unique contribution to screening in a 1D system⁵⁸. Due to the structural similarity of nanotubes and nanoribbons we believe that this explanation could work for the present material, too. Another contribution to the observed spectral function could come from the disorder in the adsorbed positive Li ions.

The Raman G band of lithium doped GNRs does not exhibit a downshift that might be expected if a Kohn anomaly at Γ point were induced upon doping. The combined investigation of the electron and phonon system allowed us to comprehensively answer this point. Since the mass renormalization is so strong, the conduction bands become flat and the Fermi wavevector k_F rapidly moves away from the apex of the conduction band parabola. This shifts the $q = 2k_F$ phonon away from the BZ center and hence out of reach of Raman spectroscopy. The combination of ARPES and Raman was also key to understand the Raman intensity decrease which is apparently not due to Pauli blocking but due to a change in the resonance condition caused by the combined effects of changes in the QP dispersion and exciton binding energy.

In conclusion, we observed changes in the electron and phonon systems in GNRs upon a semiconductor-to-metal transition have been unravelled using ARPES, STS and polarized UHV-Raman techniques. Ultra narrow GNRs are a new functional nanomaterial which can be effectively transformed from a wide-gap semiconductor into a metal via controlled lithium doping. GNRs are also a unique platform for combined experimental and theoretical studies embracing many-body interactions. The present work constitutes the first direct proof of a combined giant QP renormalization and a phonon renormalization upon charge transfer doping of a 1D material. It has a relevance for the large 1D materials community and it lays the foundations for further studies of doped GNRs.

Experimental and computational details

Experimental details

7-AGNRs were synthesized by surface polymerization of 10,10-dibromo-9,9-bianthryl (DBBA) molecules ¹⁷ on Au(111) and Au(788) surfaces. Au substrates were cleaned by three cycles of Ar⁺ sputtering (800 V) and subsequent annealing at 500 °C. The clean surface of Au(788) is shown in supplementary information. DBBA molecules were evaporated from a quartz crucible using a homebuilt evaporator with a thermocouple attached to the molecule reservoir. The deposition rate was controlled using a quartz microbalance. About 8Å of precursor molecules (using the graphite density and Z-factor) were evaporated onto the Au surface which was kept at room-temperature. Hereafter, a two-step polymerization reaction was performed: a 200°C annealing step followed by a 400°C annealing step, which induce debromization and cyclodehydrogenation reactions, respectively. The annealing was carried out using a computer controlled ramp that increased temperature over several hours. Lithium deposition (from 1 to 3 monolayers) was performed separately for ARPES, XPS and NEXAFS, UHV Raman measurements using commercial SAES getters, calibrated with quartz microbalance. The sample was kept at room temperature or at 80°K (for ARPES).

STM measurements were performed using an Omicron LT-STM with the samples held at 4.5 K in UHV. A tungsten tip was used for topography and spectroscopic measurements. Topographic images were acquired in constant current mode. dI/dV spectra were obtained using the lock-in technique where the tip bias was modulated by a 457 Hz, 10 mV (rms) sinusoidal voltage under open-feedback conditions. All STM images were processed with WSxM⁶⁶.

ARPES was carried out at the I3 beamline of the MAX IV synchrotron radiation facility (Lund, Sweden) using a Scienta R-4000 hemispherical electron analyser. The ARPES spectra were measured using a photon energy of 32 eV in the 2^{nd} BZ of the GNRs and shifted back by application of the reciprocal lattice vector to the 1^{st} BZ. The samples for

ARPES measurements were synthesized and checked in the UHV Raman chamber and then transferred under UHV conditions into a special container which was filled then to a slight overpressure (1.1 bar) by high purity Ar gas. Samples in UHV tight vacuum suitcases filled with an Ar were transported to the load-lock chamber of the ARPES beamline endstation and later gently annealed (at 200°C) under UHV conditions. This method allowed us to achieve reproducible experimental results.

UHV-Raman was performed in the back-scattering geometry using commercial Raman systems (Renishaw and OceanOptics) integrated in a homebuilt optical chamber where the exciting and Raman scattered light were coupled into the vacuum using a long-working distance microscope objective with an NA of ~0.4. The laser power on the sample was kept below 1 mW. The analysis chamber of the UHV-Raman is attached to another chamber for sample preparation where the 7-AGNR synthesis, LEED characterization and Li deposition were performed. Raman spectra were calibrated using Si peak at 520.5 cm⁻¹ as well as oxygen peak at 1555 cm⁻¹. Polarized Raman measurements were also performed in-situ. A half-wave plate was used to rotate polarization of the laser beam. To collect a certain polarization of the Raman light, a polarizer and a half-wave plate were inserted before the detector.

XPS and NEXAFS experiments were performed at the German-Russian beamline (RGBL) of the BESSY II synchrotron radiation facility (Berlin, Germany). XPS spectra were measured with photon energy of 320 eV and pass energy of 10 eV in the normal emission geometry. Samples were synthesized in the UHV Raman system and transferred to the synchrotron in the same manner as described for ARPES measurements. XPS data indicated no trace of oxygen as confirmed by the absence of an O1s peak at 650 eV photon energy. All XPS spectra were calibrated using the Au 4f7/2 core level at a binding energy 84.0 eV. NEXAFS data were obtained in total electron yield mode with an energy resolution of 50 meV close to the C K-edge.

Computational details

Our first-principles calculations have been performed in the framework of the density functional theory⁶⁷ by using pseudopotentials obtained the projector augmented wave method? and the Perdew-Burke-Ernzerhof exchange-correlation energy functional? as implemented in the Vienna ab initio simulation package code?? The ground-state adsorption geometry of Li on the C₁₄H₄ nanoribbon was obtained for an energy cutoff of 500 eV and by including the van der Waals interactions with the help of the non-local correlation energy functional vdW-DF2? together with the exchange energy functional developed by Hamada? The phonon energy dispersion relation was calculated using a modified fourth-nearest neighbor force constant model that has been used for graphene previously⁵². The difference lies in the larger unit cell for 7-AGNRs (14 carbon atoms), and due to the small ribbon width many carbon-carbon interactions become equal to zero.

Acknowledgements

B.S. and A.G. acknowledge the ERC grant no. 648589 'SUPER-2D', funding from Quantum Matter and Materials and DFG project GR 3708/2-1. N.I.V. acknowledges the Russian Science Foundation (No. 14-13-00747). Research supported by the U.S. Department of Energy (DOE), Office of Science, Basic Energy Sciences (BES), under Award no. DE-SC0010409 (design, synthesis and characterization of molecular building blocks) and the Center for Energy Efficient Electronics Science NSF Award 0939514 (SPM imaging and spectroscopy). K.S. and A.P. acknowledge support from the Swedish Research Council and the ERC grant no. 321319.

References

1. Ishii, H.; Kataura, H.; Shiozawa, H.; Yoshioka, H.; Otsubo, H.; Takayama, Y.; Miyahara, T.; Suzuki, S.; Achiba, Y.; Nakatake, M. et al. Direct observation of Tomonaga-

- Luttinger-liquid state in carbon nanotubes at low temperatures. *Nature* **2003**, *426*, 540–544.
- Kim, B. J.; Koh, H.; Rotenberg, E.; Oh, S.-J.; Eisaki, H.; Motoyama, N.; Uchida, S.; Tohyama, T.; Maekawa, S.; Shen, Z.-X. et al. Distinct spinon and holon dispersions in photoemission spectral functions from one-dimensional SrCuO₂. Nature Physics 2006, 2, 397–401.
- Ahn, J. R.; Kang, P. G.; Ryang, K. D.; Yeom, H. W. Coexistence of Two Different Peierls Distortions within an Atomic Scale Wire: Si(553)-Au. Phys. Rev. Lett. 2005, 95, 196402.
- 4. Wang, F.; Dukovic, G.; Brus, L.; Heinz, T. The Optical Resonances in Carbon Nanotubes Arise from Excitons. *Science* **2005**, *308*, 838.
- 5. Yang, L.; Park, C.-H.; Son, Y.-W.; Cohen, M. L.; Louie, S. G. Quasiparticle Energies and Band Gaps in Graphene Nanoribbons. *Phys. Rev. Lett.* **2007**, *99*, 186801.
- 6. Prezzi, D.; Varsano, D.; Ruini, A.; Marini, A.; Molinari, E. Optical properties of graphene nanoribbons: The role of many-body effects. *Phys. Rev. B* **2008**, *77*, 041404.
- 7. Prezzi, D.; Varsano, D.; Ruini, A.; Molinari, E. Quantum dot states and optical excitations of edge-modulated graphene nanoribbons. *Phys. Rev. B* **2011**, *84*, 041401.
- 8. Ruffieux, P.; Cai, J.; Plumb, N. C.; Patthey, L.; Prezzi, D.; Ferretti, A.; Molinari, E.; Feng, X.; Müllen, K.; Pignedoli, C. A. *et al.* Electronic Structure of Atomically Precise Graphene Nanoribbons. *ACS Nano* **2012**, *6*, 6930–6935, PMID: 22853456.
- Denk, R.; Hohage, M.; Zeppenfeld, P.; Cai, J.; Pignedoli, C. A.; Söde, H.; Fasel, R.;
 Feng, X.; Müllen, K.; Wang, S. et al. Exciton-dominated optical response of ultra-narrow graphene nanoribbons. Nat. Commun. 2014, 5, 4253.

- 10. Lee, J. U. Band-gap renormalization in carbon nanotubes: Origin of the ideal diode behavior in carbon nanotube *p-n* structures. *Phys. Rev. B* **2007**, *75*, 075409.
- Steiner, M.; Freitag, M.; Perebeinos, V.; Naumov, A.; Small, J. P.; Bol, A. A.; Avouris, P. Gate-Variable Light Absorption and Emission in a Semiconducting Carbon Nanotube.
 Nano Letters 2009, 9, 3477–3481, PMID: 19637914.
- Hartleb, H.; Späth, F.; Hertel, T. Evidence for Strong Electronic Correlations in the Spectra of Gate-Doped Single-Wall Carbon Nanotubes. ACS Nano 2015, 9, 10461– 10470, PMID: 26381021.
- 13. Miyauchi, Y.; Zhang, Z.; Takekoshi, M.; Tomio, Y.; Suzuura, H.; Perebeinos, V.; Deshpande, V. V.; Lu, C.; Berciaud, S.; Kim, P. et al. Tunable electronic correlation effects in nanotube-light interactions. *Phys. Rev. B* **2015**, *92*, 205407.
- 14. Sanchez-Valencia, J. R.; Dienel, T.; Gröning, O.; Shorubalko, I.; Mueller, A.; Jansen, M.; Amsharov, K.; Ruffieux, P.; Fasel, R. Controlled synthesis of single-chirality carbon nanotubes. *Nature* **2014**, *512*, 61–64.
- 15. Bae, S.; Kim, H.; Lee, Y.; Xu, X.; Park, J.-S.; Zheng, Y.; Balakrishnan, J.; Lei, T.; Ri Kim, H.; Song, Y. I. *et al.* Roll-to-roll production of 30-inch graphene films for transparent electrodes. *Nat Nano* **2010**, *5*, 574–578.
- 16. Grill, L.; Dyer, M.; Lafferentz, L.; Persson, M.; Peters, M. V.; Hecht, S. Nano-architectures by covalent assembly of molecular building blocks. *Nature Nanotechnology* **2007**, 2, 687–691.
- 17. Cai, J.; Ruffieux, P.; Jaafar, R.; Bieri, M.; Braun, T.; Blankenburg, S.; Muoth, M.; Seitsonen, A. P.; Saleh, M.; Feng, X. *et al.* Atomically precise bottom-up fabrication of graphene nanoribbons. *Nature* **2010**, *466*, 470–473.

- 18. Koch, M.; Ample, F.; Joachim, C.; Grill, L. Voltage-dependent conductance of a single graphene nanoribbon. *Nature Nano* **2012**, *7*, 713–717.
- Chen, Y.-C.; de Oteyza, D. G.; Pedramrazi, Z.; Chen, C.; Fischer, F. R.; Crommie, M. F. Tuning the Band Gap of Graphene Nanoribbons Synthesized from Molecular Precursors. ACS Nano 2013, 7, 6123–6128, PMID: 23746141.
- Cloke, R. R.; Marangoni, T.; Nguyen, G. D.; Joshi, T.; Rizzo, D. J.; Bronner, C.; Cao, T.;
 Louie, S. G.; Crommie, M. F.; Fischer, F. R. Site-Specific Substitutional Boron Doping of Semiconducting Armchair Graphene Nanoribbons. *Journal of the American Chemical Society* 2015, 137, 8872–8875, PMID: 26153349.
- Kawai, S.; Saito, S.; Osumi, S.; Yamaguchi, S.; Foster, A. S.; Spijker, P.; Meyer, E. Atomically controlled substitutional boron-doping of graphene nanoribbons. *Nat. Commun.* 2015, 6, 8098.
- 22. Kimouche, A.; Ervasti, M. M.; Drost, R.; Halonen, S.; Harju, A.; Joensuu, P. M.; Sainio, J.; Liljeroth, P. Ultra-narrow metallic armchair graphene nanoribbons. *Nat. Commun.* **2015**, *6*, 10177.
- 23. Ruffieux, P.; Wang, S.; Yang, B.; Sànchez-Sànchez, C.; Liu, J.; Dienel, T.; Talirz, L.; Shinde, P.; Pignedoli, C. A.; Passerone, D. et al. On-surface synthesis of graphene nanoribbons with zigzag edge topology. Nature 2016, 531, 489492.
- 24. Han, M. Y.; Ozyilmaz, B.; Zhang, Y.; Kim, P. Energy Band-Gap Engineering of Graphene Nanoribbons. *Phys. Rev. Lett.* **2007**, *98*, 206805.
- 25. Barone, V.; Hod, O.; Scuseria, G. E. Electronic Structure and Stability of Semiconducting Graphene Nanoribbons. *Nano Letters* **2006**, *6*, 2748–2754, PMID: 17163699.
- 26. Chen, Y.-C.; Cao, T.; Chen, C.; Pedramrazi, Z.; Haberer, D.; D.G. de Oteyza, S. L., F.R. Fischer; Crommie, M. Molecular bandgap engineering of bottom-

- up synthesized graphene nanoribbon heterojunctions. Nature Nanotechnology **2015**, 10, 156160.
- 27. Chen, Z.; Lin, Y.-M.; Rooks, M. J.; Avouris, P. Graphene nano-ribbon electronics. Physica E: Low-dimensional Systems and Nanostructures 2007, 40, 228 232, International Symposium on Nanometer-Scale Quantum Physics.
- Wang, X.; Ouyang, Y.; Li, X.; Wang, H.; Guo, J.; Dai, H. Room-Temperature All-Semiconducting Sub-10-nm Graphene Nanoribbon Field-Effect Transistors. *Phys. Rev. Lett.* 2008, 100, 206803.
- 29. Schwierz, F. Graphene transistors. Nature Nanotechnology 2010, 5, 487496.
- 30. Li, X.; Wang, X.; Zhang, L.; Lee, S.; Dai, H. Chemically Derived, Ultrasmooth Graphene Nanoribbon Semiconductors. *Science* **2008**, *319*, 1229–1232.
- 31. Liao, L.; Bai, J.; Cheng, R.; Lin, Y.-C.; Jiang, S.; Huang, Y.; Duan, X. Top-Gated Graphene Nanoribbon Transistors with Ultrathin High-k Dielectrics. *Nano Letters* **2010**, 10, 1917–1921.
- 32. Linden, S.; Zhong, D.; Timmer, A.; Aghdassi, N.; Franke, J. H.; Zhang, H.; Feng, X.; Müllen, K.; Fuchs, H.; Chi, L. et al. Electronic Structure of Spatially Aligned Graphene Nanoribbons on Au(788). Phys. Rev. Lett. 2012, 108, 216801.
- 33. Ahn, J. R.; Byun, J. H.; Koh, H.; Rotenberg, E.; Kevan, S. D.; Yeom, H. W. Mechanism of Gap Opening in a Triple-Band Peierls System: In Atomic Wires on Si. *Phys. Rev. Lett.* **2004**, *93*, 106401.
- 34. Cervantes-Sodi, F.; Csányi, G.; Piscanec, S.; Ferrari, A. C. Edge-functionalized and substitutionally doped graphene nanoribbons: Electronic and spin properties. *Phys. Rev.* B 2008, 77, 165427.

- 35. Yan, Q.; Huang, B.; Yu, J.; Zheng, F.; Zang, J.; Wu, J.; Gu, B.-L.; Liu, F.; ; Duan, W. Intrinsic CurrentVoltage Characteristics of Graphene Nanoribbon Transistors and Effect of Edge Doping. *Nano Letters* **2007**, *7*, 1469–1473.
- 36. Wang, X.; Li, X.; Zhang, L.; Yoon, Y.; Weber, P. K.; Wang, H.; Guo, J.; Dai, H. N-Doping of Graphene Through Electrothermal Reactions with Ammonia. *Science* **2009**, 324, 768–771.
- 37. Rosenkranz, N.; Till, C.; Thomsen, C.; Maultzsch, J. *Ab initio* calculations of edge-functionalized armchair graphene nanoribbons: Structural, electronic, and vibrational effects. *Phys. Rev. B* **2011**, *84*, 195438.
- 38. Martins, T. B.; Miwa, R. H.; da Silva, A. J. R.; Fazzio, A. Electronic and Transport Properties of Boron-Doped Graphene Nanoribbons. *Phys. Rev. Lett.* **2007**, *98*, 196803.
- 39. Tan, Y.-Z.; Yang, B.; Parvez, K.; Narita, A.; Osella, S.; Beljonne, D.; Feng, X.; Müllen, K. Atomically precise edge chlorination of nanographenes and its application in graphene nanoribbons. *Nat. Commun.* **2013**, *4*, 2646.
- 40. Bronner, C.; Stremlau, S.; Gille, M.; Brauße, F.; Haase, A.; Hecht, S.; Tegeder, P. Aligning the Band Gap of Graphene Nanoribbons by Monomer Doping. *Angewandte Chemie International Edition* **2013**, *52*, 4422–4425.
- 41. Cloke, R. R.; Marangoni, T.; Nguyen, G. D.; Joshi, T.; Rizzo, D. J.; Bronner, C.; Cao, T.; Louie, S. G.; Crommie, M. F.; Fischer, F. R. Site-Specific Substitutional Boron Doping of Semiconducting Armchair Graphene Nanoribbons. *Journal of the American Chemical Society* 2015, 137, 8872–8875, PMID: 26153349.
- 42. Haberer, D.; Petaccia, L.; Fedorov, A. V.; Praveen, C. S.; Fabris, S.; Piccinin, S.; Vilkov, O.; Vyalikh, D. V.; Preobrajenski, A.; Verbitskiy, N. I. *et al.* Anisotropic Eliashberg function and electron-phonon coupling in doped graphene. *Phys. Rev. B* **2013**, *88*, 081401.

- 43. Fedorov, A. V.; Verbitskiy, N. I.; Haberer, D.; Struzzi, C.; Petaccia, L.; Usachov, D.; Vilkov, O. Y.; Vyalikh, D. V.; Fink, J.; Knupfer, M. et al. Observation of a universal donor-dependent vibrational mode in graphene. Nat. Commun. 2014, 5, 4257.
- 44. Ludbrook, B. M.; Levy, G.; Nigge, P.; Zonno, M.; Schneider, M.; Dvorak, D. J.; Veenstra, C. N.; Zhdanovich, S.; Wong, D.; Dosanjh, P. et al. Evidence for superconductivity in Li-decorated monolayer graphene. *Proceedings of the National Academy of Sciences* **2015**, *112*, 11795–11799.
- 45. Chapman, J.; Su, Y.; Howard, C. A.; Kundys, D.; Grigorenko, A. N.; Guinea, F.; Geim, A. K.; Grigorieva, I. V.; Nair, R. R. Superconductivity in Ca-doped graphene laminates. *Scientific Reports* **2016**, *6*, 23254.
- 46. Rauf, H.; Pichler, T.; Knupfer, M.; Fink, J.; Kataura, H. Transition from a Tomonaga-Luttinger Liquid to a Fermi Liquid in Potassium-Intercalated Bundles of Single-Wall Carbon Nanotubes. *Phys. Rev. Lett.* **2004**, *93*, 096805.
- 47. Repain, V.; Baudot, G.; Ellmer, H.; Rousset, S. Two-dimensional long-rangeordered growth of uniform cobalt nanostructures on a Au(111) vicinal template. *Europhysics Letters* **2002**, *58*, 730.
- 48. Wofford, J. M.; Starodub, E.; Walter, A. L.; Nie, S.; Bostwick, A.; Bartelt, N. C.; Thrmer, K.; Rotenberg, E.; McCarty, K. F.; Dubon, O. D. Extraordinary epitaxial alignment of graphene islands on Au(111). *New Journal of Physics* **2012**, *14*, 053008.
- 49. Varykhalov, A.; Scholz, M. R.; Kim, T. K.; Rader, O. Effect of noble-metal contacts on doping and band gap of graphene. *Phys. Rev. B* **2010**, *82*, 121101.
- 50. Sasaki, K.; Kato, K.; Tokura, Y.; Oguri, K.; Sogawa, T. Theory of optical transitions in graphene nanoribbons. *Phys. Rev. B* **2011**, *84*, 085458.

- Duesberg, G. S.; Loa, I.; Burghard, M.; Syassen, K.; Roth, S. Polarized Raman Spectroscopy on Isolated Single-Wall Carbon Nanotubes. *Phys. Rev. Lett.* 2000, 85, 5436–5439.
- 52. Saito, R.; Dresselhaus, G.; Dresselhaus, M. S. *Physical Properties of Carbon Nanotubes*; Imperial College Press: London, 1998.
- 53. Sanders, G. D.; Nugraha, A. R. T.; Saito, R.; Stanton, C. J. Coherent radial-breathing-like phonons in graphene nanoribbons. *Phys. Rev. B* **2012**, *85*, 205401.
- 54. Söde, H.; Talirz, L.; Gröning, O.; Pignedoli, C. A.; Berger, R.; Feng, X.; Müllen, K.; Fasel, R.; Ruffieux, P. Electronic band dispersion of graphene nanoribbons via Fourier-transformed scanning tunneling spectroscopy. *Phys. Rev. B* **2015**, *91*, 045429.
- 55. Nakada, K.; Fujita, M.; Dresselhaus, G.; Dresselhaus, M. S. Edge state in graphene ribbons: Nanometer size effect and edge shape dependence. *Phys. Rev. B* 1996, 54, 17954–17961.
- 56. Ezawa, M. Peculiar width dependence of the electronic properties of carbon nanoribbons. *Phys. Rev. B* **2006**, *73*, 045432.
- 57. Son, Y.-W.; Cohen, M. L.; Louie, S. G. Energy Gaps in Graphene Nanoribbons. *Phys. Rev. Lett.* **2006**, *97*, 216803.
- 58. Spataru, C. D.; Léonard, F. Tunable Band Gaps and Excitons in Doped Semiconducting Carbon Nanotubes Made Possible by Acoustic Plasmons. Phys. Rev. Lett. 2010, 104, 177402.
- 59. Vasseur, G.; Fagot-Revurat, Y.; Sicot, M.; Kierren, B.; Moreau, L.; Malterre, D.; Cardenas, L.; Galeotti, G.; Lipton-Duffin, J.; Rosei, F. et al. Quasi one-dimensional band dispersion and surface metallization in long-range ordered polymeric wires. Nat Commun 2016, 7, 10235.

- 60. Ugeda, M. M.; Bradley, A. J.; Shi, S.-F.; da Jornada, F. H.; Zhang, Y.; Qiu, D. Y.; Ruan, W.; Mo, S.-K.; Hussain, Z.; Shen, Z.-X. et al. Giant bandgap renormalization and excitonic effects in a monolayer transition metal dichalcogenide semiconductor. Nature Materials 2014, 13, 1091–1095.
- 61. Kuzmany, H.; Plank, W.; Hulman, M.; Kramberger, C.; Grüneis, A.; Pichler, T.; Peterlik, H.; Kataura, H.; Achiba, Y. Determination of SWCNT diameters from the Raman response of the radial breathing mode. *Euro. Phys. J. B* **2001**, *22*, 307–320.
- 62. Pisana, S.; Lazzeri, M.; Casiraghi, C.; Novoselov, K.; Geim, A.; Ferrari, A.; Mauri, F. Breakdown of the adiabatic Born-Oppenheimer approximation in graphene. Nat. Mat. 2007, 6, 198.
- 63. Yan, J.; Zhang, Y.; Kim, P.; Pinczuk, A. Electric Field Effect Tuning of Electron-Phonon Coupling in Graphene. *Phys. Rev. Lett.* **2007**, *98*, 166802.
- 64. Das, A.; Pisana, S.; Chakraborty, B.; Piscanec, S.; Saha, S. K.; Waghmare, U. V.; Novoselov, K. S.; Krishnamurthy, H. R.; Geim, A. K.; Ferrari, A. C. et al. Monitoring dopants by Raman scattering in an electrochemically top-gated graphene transistor. Nature Nanotechnology 2008, 3, 210–215.
- 65. Chakraborty, B.; Bera, A.; Muthu, D. V. S.; Bhowmick, S.; Waghmare, U. V.; Sood, A. K. Symmetry-dependent phonon renormalization in monolayer MoS₂ transistor. *Phys. Rev. B* **2012**, *85*, 161403.
- 66. Horcas, I.; Fernandez, R.; Gomez-Rodriguez, J.; Colchero, J.; Gomez-Herrero, J.; Baro, A. WSXM: A software for scanning probe microscopy and a tool for nanotechnology. Review of Scientific Instruments 2007, 78, 013705.
- 67. Kohn, W.; Sham, L. J. Self-Consistent Equations Including Exchange and Correlation Effects. *Phys. Rev.* **1965**, *140*, A1133–A1138.